Plasmon-Enhanced Photoelectrochemical Water Splitting with Size-Controllable Gold Nanodot Arrays

Hyung Ju Kim,[†,⊥] Sang Ho Lee,[‡,⊥] Aniruddha A. Upadhye,[†] Insoo Ro,[†] M. Isabel Tejedor-Tejedor,[§] Marc A. Anderson,[§] Won Bae Kim,[*,‡] and George W. Huber[*,†]

[†]Department of Chemical and Biological Engineering, University of Wisconsin—Madison, 1415 Engineering Drive, Madison, Wisconsin 53706, United States, [‡]School of Materials Science and Engineering, Research Institute for Solar and Sustainable Energies, Gwangju Institute of Science and Technology, 261 Cheomdan-gwagiro, Buk-gu, Gwangju 500-712, South Korea, and [§]Department of Civil and Environmental Engineering, University of Wisconsin—Madison, 660 North Park Street, Madison, Wisconsin 53706, United States. [⊥]H. J. Kim and S. H. Lee contributed equally to this work.

ABSTRACT Size-controllable Au nanodot arrays (50, 63, and 83 nm dot size) with a narrow size distribution (±5%) were prepared by a direct contact printing method on an indium tin oxide (ITO) substrate. Titania was added to the Au nanodots using TiO_2 sols of 2−3 nm in size. This created a precisely controlled Au nanodot with 110 nm of TiO_2 overcoats. Using these precisely controlled nanodot arrays, the effects of Au nanodot size and TiO_2 overcoats were investigated for photoelectrochemical water splitting using a three-electrode system with a fiber-optic visible light source. From UV—vis measurement, the localized surface plasmon resonance (LSPR) peak energy (E_{LSPR}) increased and the LSPR line width (Γ) decreased with decreasing Au nanodot size. The generated plasmonic enhancement for the photoelectrochemical water splitting reaction increased with decreasing Au particle size. The measured plasmonic enhancement for light on/off experiments was 25 times for the 50 nm Au size and 10 times for the 83 nm Au nanodot size. The activity of each catalyst increased by a factor of 6 when TiO_2 was added to the Au nanodots for all the samples. The activity of the catalyst was proportional to the quality factor (defined as $Q = E_{LSPR}/\Gamma$) of the plasmonic metal nanostructure. The enhanced water splitting performance with the decreased Au nanodot size is probably due to more generated charge carriers (electron/hole pair) by local field enhancement as the quality factor increases.

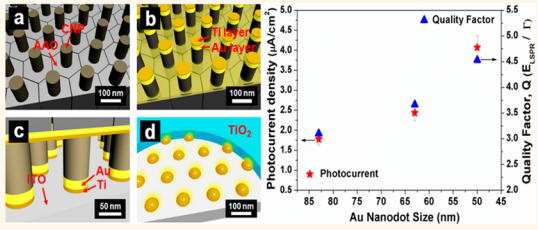

KEYWORDS: plasmonic water splitting · Au nanodot · contact printing method · Au-TiO_2 catalyst · quality factor

The direct conversion of solar to chemical energy using photocatalysts in an economical way would allow society to reduce its dependence on fossil-based fuels and move toward a more sustainable economy. One option for solar conversion to chemical energy is the photocatalytic splitting of water with semiconductor oxides such as TiO_2.[1−6] In TiO_2, an absorbed photon generates an electron/hole (e^-/h^+) pair. In photocatalytic water splitting, the created holes (h^+) drive the oxygen-evolution reaction (at high pH, $4OH^- + 4h^+ \rightarrow 2H_2O + O_2$), whereas the electrons (e^-) participate in the hydrogen-evolution reaction (at high pH, $4H_2O + 4e^- \rightarrow 4OH^- + 2H_2$). While TiO_2 is both stable and inexpensive, the main limitation of using TiO_2 is that it does not absorb visible light.[7−10] One approach to increase the visible light absorption in the TiO_2-based systems is to add plasmonic metal particles to the TiO_2, such as Au, Ag, and Cu. These metals absorb visible light through localized surface plasmon resonance (LSPR). Surface plasmons are collective oscillations of the free charge confined to the surfaces of conducting metals that interact strongly with light.[7−13] The frequency at which the conduction electrons oscillate in a metal nanoparticle is called the LSPR frequency.[8,10,14] The LSPR frequency depends on the metal's size, shape, and environment.[11−22] Several attempts have been made to synthesize plasmonic metal—semiconductor systems such as Au/TiO_2 for

* Address correspondence to huber@engr.wisc.edu; wbkim@gist.ac.kr.

Received for review August 11, 2014 and accepted September 30, 2014.

Published online September 30, 2014
10.1021/nn504484u

the photocatalytic water splitting reaction by controlling the structure and concentration of plasmonic metals[23−26] and by modifying the semiconductor oxides with defects.[27] The size of the plasmonic metal particles can tune the LSPR frequency, which gives rise to changes of LSPR spectral line shape (*i.e.*, absorption peak shape in the visible range).[15−19,21,22,28−30] The spectral line shape of the LSPR in any metallic nanosystem, as obtained when measuring absorption as a function of photon energy, can be analyzed by the LSPR peak energies (spectral peak position) and the LSPR line widths (full line width at half-maximum of spectral peak), assuming that the metals are very similar in size.[19,21,22,28] However, the challenge with most previous studies is that the plasmonic metals have a wide range of particle size distribution, making the analysis of the LSPR complicated.[16,31] The changes of LSPR peak energy and LSPR line width with different metal size can affect the local field enhancement on the plasmonic metallic nanosystem.[14,21,28] It has also been demonstrated that the intense local electric field near the surface of plasmonic nanoparticles can increase the e^-/h^+ pair generation rate at the metal/semiconductor interface, improving the water splitting performance.[23,27] Precise size control of the plasmonic metal with narrow size distribution is critical to see the exact size effect for the water splitting performance.

Contact printing is a recently developed method that has been used to synthesize precisely controlled metal nanostructures.[32−35] This approach is gaining attention in the field of nanofabrication because of its simplicity, versatility, low cost, and high throughput.[32,33] Using the printing strategy, a wide range of nanostructures, such as complicated pattern designs and three-dimensional (3D) stacks, have been synthesized on various substrates.[36−38] The printing technology is based on the transfer of materials loaded on stamp patterns to substrate surfaces by intimate contact between the stamp and substrate. This enables uniform metal nanostructure arrays to be efficiently synthesized over various substrate substances and their size, interval, and density to be readily controlled with a narrow deviation. Using these nanostructure arrays, a better relationship between the metal nanostructures and their performance in a reaction can be developed.

In this article, printable plasmonic metal nanostructures made by direct contact printing are used to investigating the size effect of Au on the water splitting reaction. Size-controllable Au nanodot arrays are directly printed onto indium tin oxide (ITO) glasses by stamps of vertically aligned carbon nanopost (CNP) arrays that are supported within porous channels of anodic aluminum oxide (AAO) templates. The size of the printed Au nanodots can be precisely adjusted by controlling the geometry of the stamp tips. This method produces Au nanodots with a narrow size distribution (±5%). Here, we demonstrate that the quality factor, defined as LSPR peak energy divided by LSPR line width, increases as contact-printed Au nanodot size decreases from 83 nm to 50 nm. As we will demonstrate in this paper, the quality factor is proportional to the rate enhancement for photoelectrochemical water splitting.

RESULTS AND DISCUSSION

Figure 1a−d illustrate the fabrication of the Au nanodot arrays on the ITO substrate. For printing of the controlled Au nanodots, CNP stamps were employed in this work (see Figure S1 for the synthesis of a CNP stamp). These stamping platforms consist of vertical one-dimensional carbon nanopost arrays with

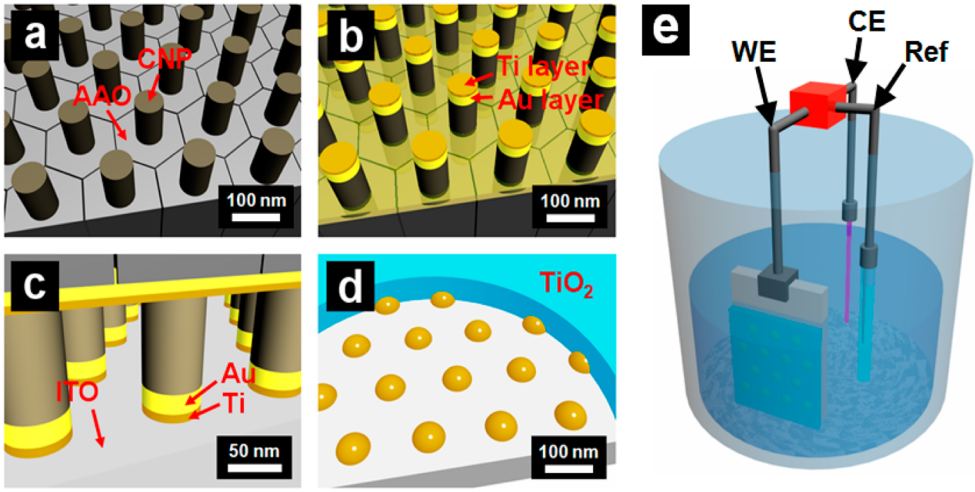

Figure 1. Schematic illustrations depict the entire fabrication process for TiO_2-coated Au nanodot arrays and the plasmonic-enhanced water splitting reactor: (a) preparation of the carbon nanopost (CNP) stamp, (b) loading of the Au metal and Ti adhesion layers on the CNP tips, (c) contact printing of the metal-loaded stamp onto ITO glasses, (d) formation of the Au nanodot arrays and the TiO_2-coated Au nanodot arrays, and (e) photoelectrochemical water splitting reactor used in this work.

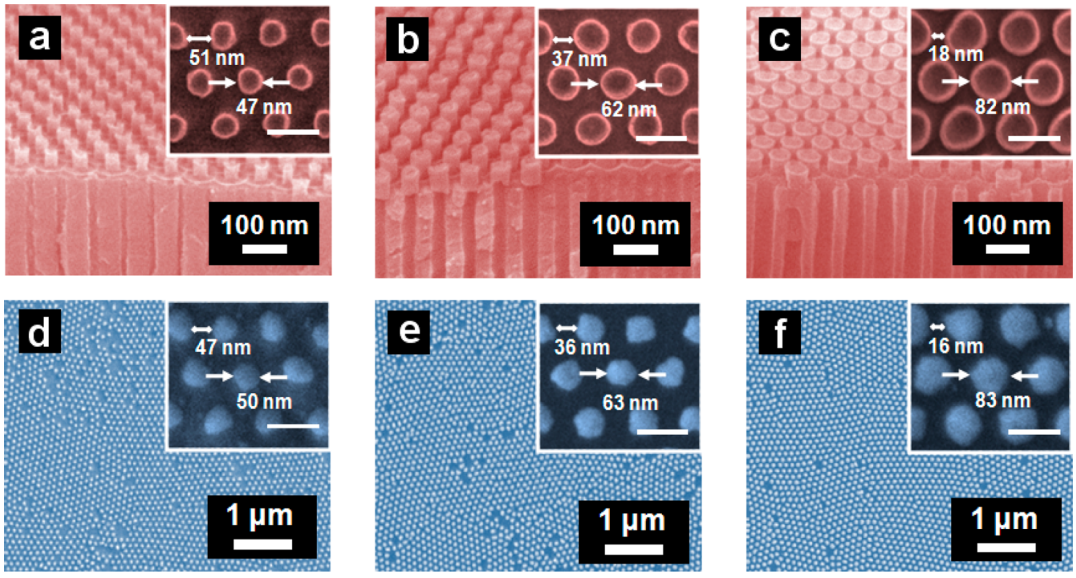

Figure 2. SEM images of prepared Au nanodot arrays. SEM images of (a−c) the CNP stamps with controlled tip diameter and (d−f) the printed Au nanodot arrays with controlled size. All the insets show magnified SEM images, and all scale bars in the insets are 100 nm.

circular tips, which are supported by the hexagonally aligned pore channels of the AAO matrices (Figure 1a). Also, the tip size and interval of the stamps can be precisely adjusted by controlling the pore dimensions of the mother AAO molds. Thus, the diameter of the printed plasmonic Au nanodot arrays can be systematically tuned in tight correspondence with the stamp geometries. The metallic Au layers to be printed are then deposited on the tips of the CNP stamps by an electron-beam (e-beam) or thermal evaporation process (Figure 1b). Transfer of the metal layers from the stamp tips to the substrate surfaces is related to the different adhesion strengths of the metal between the stamps and substrate surfaces. For the successful printing of metal nanodot arrays, the cohesion force of the metal layers to the substrates should be much higher than the force of the metals to the stamp tips when the metal-loaded stamps are brought into contact with the substrates.[39] In this study, a thin Ti layer (*ca.* 1 nm) was introduced to enhance the adhesion force of the Au layer to the substrates. Next, the Au metal-loaded stamps are printed onto the ITO substrate surfaces under a proper pressure (Figure 1c). After lifting the stamps from the substrates, plasmonic Au nanodot arrays are formed over the ITO substrates. A TiO_2 layer was coated on the printed Au plasmonic particles by dip-coating the Au nanodot arrays on the ITO substrate into a TiO_2 sol solution (Figure 1d). The electrodes were finally prepared by an annealing process at 300 °C in an oven for 1 h. The TiO_2-coated Au nanodot arrays were directly used as working electrodes in the photoelectrochemical water splitting reactor (Figure 1e). A Pt wire and Ag/AgCl (in sat. KCl) were used as counter and reference electrodes, respectively. The gas phase was analyzed using a Shimadzu GC-2010 Plus system with a barrier ionization discharge detector.

Figure 2a−c exhibit scanning electron microscope (SEM) images of the CNP stamps used in this work. The circular CNP tips are hexagonally aligned by alumina templates. As seen in the inset images of Figure 2a−c, the size and interval of the CNP stamps can be adjusted by controlling the pore dimension of the templates. As the tip size of the nanostamps increased from *ca.* 47 nm to *ca.* 82 nm, the distance between the CNPs was systematically modified from *ca.* 51 nm to *ca.* 18 nm. This results in tuning the diameter and spacing of the printed Au nanodot arrays. Vertical CNP arrays with a high tip density (*ca.* 1×10^{10} cm^{-2}) are also firmly supported by AAO templates. This can alleviate the structural deformation of the CNP tip morphologies when external pressure is applied for conformal contact between the stamp and substrate surfaces during contact printing, which can permit the CNP stamps to be reused several times. Figure 2d−f display the printed Au nanodot array with the controlled diameter and interval. By controlling the tip dimensions of the mother stamps, the diameter of the printed Au nanodots was tuned from *ca.* 50 nm to *ca.* 83 nm, and the interdistance between the printed dots was also modified from *ca.* 47 nm to *ca.* 16 nm. Some discrepancy between the sizes of the stamp tips and the printed Au dots exists, which might be attributed to the increased size of the metal-loaded stamps after metal layer deposition (see Figure S2). Nevertheless, the diameter of the printed Au nanodots shows close correspondence with the size of the CNP tips. In addition, the printed Au nanodot arrays have narrow size distributions (±5%), which were not affected by the size of the nanodots (Figure S3). Figure S4 shows the

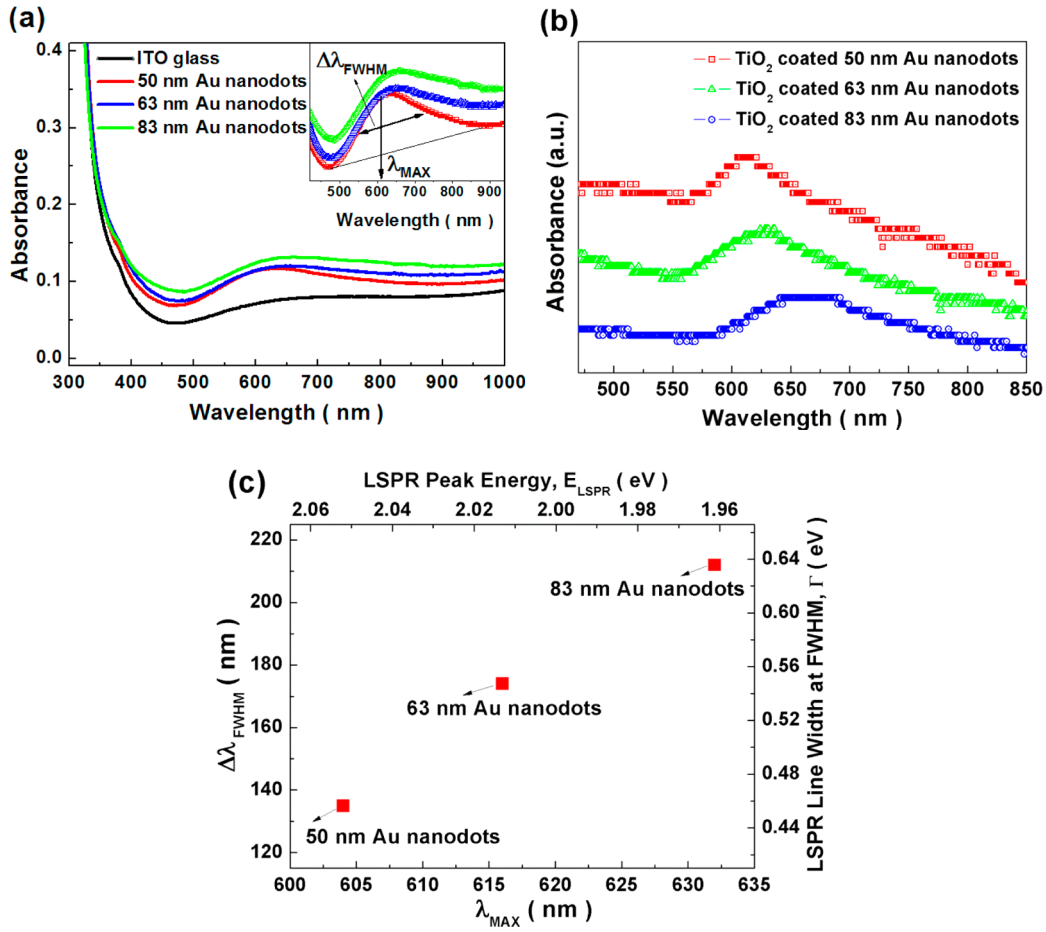

Figure 3. Optical properties of Au nanodot arrays. (a) UV−vis absorption spectra of 50, 63, and 83 nm Au nanodots on ITO glass. (b) UV−vis absorption spectra of TiO_2-coated 50, 63, and 83 nm Au nanodots on ITO glass. The figure shows difference spectra for Au nanodots (*i.e.*, the spectrum of TiO_2-coated Au nanodots on ITO glass minus the spectrum of TiO_2-coated ITO glass). (c) LSPR peak energy (E_{LSPR}) and dot size dependence of the LSPR line width (Γ) for Au nanodots as obtained from the UV−vis measurements.

representative SEM, X-ray diffraction (XRD), and X-ray photoelectron spectroscopy (XPS) data for Au nanodots printed on ITO substrates. In Figure S4a, the oblate spheroidal Au nanodots (height: 12 nm, diameter: 50 nm) are well aligned with the patterns of the CNP stamps. The height of the printed Au nanodots corresponded almost exactly to the thickness of metal layers that were loaded on the tips of the CNP stamps before contact printing. In this work, the height of 63 nm diameter Au nanodots is approximately 13 nm, while that of 83 nm diameter nanodots is approximately 15 nm. In Figure S4b, the printed Au nanodots exhibit a typical (111) face-centered cubic lattice structure. No extra diffraction peaks, excluding those from the main lattices of Au metal ($2\theta = 38°$) and ITO, were observed, indicating that the Au dot arrays were successfully printed on the ITO glasses without impurities. In Figure S4c,d, XPS analysis of the Au nanodot arrays printed on ITO glass clearly confirms that the Au/Ti interface formed around the perimeter of Au nanodots. Figure S5a shows a surface SEM image after coating of a TiO_2 layer on the printed Au nanodot using the sol−gel process. After coating of the TiO_2 layers, an embossing-like morphology is produced, which might be ascribed to the formation of a TiO_2 layer by the thermal annealing process.[40−42] The thickness of the coated TiO_2 layers is *ca.* 110 nm, which was estimated by the tilted SEM image in Figure S5b. The XRD investigation for the TiO_2 indicates that anatase is predominant (Figure S5c). The particle size of the TiO_2 sol was 2−3 nm in diameter as measured by XRD (Table S1). As shown in Figure S5d, the Barrett−Joyner−Halenda pore-size distribution demonstrates that the TiO_2 layer is mesoporous with an average pore size of 3.4 nm.

The optical properties of prepared Au nanodot arrays are shown in Figure 3. Figure 3a shows the UV−vis absorption spectra of Au nanodots with diameters of 50, 63, and 83 nm on ITO glass. As shown in Figure 3a, the plasmon absorption for all the prepared Au nanodots is clearly seen in the visible region. The plasmon resonance wavelength (λ_{MAX}) experiences a red-shift as the Au nanodot size increases from 50 nm to 83 nm. It is well known that there is

a red spectral shift with increasing Au nanoparticle size.[15−18,21,22,28,29,43] The λ_{MAX} of the Au nanoparticles also depends on spacing between the particles.[29,44] As shown in Figure 2, the interdistance between the printed dots decreased from 47 nm to 16 nm with an increase of dot size from 50 nm to 83 nm. The λ_{MAX} red-shifts as the dot size increases and the interdistance decreases as shown in Figure 3a. This observed behavior can also be explained by the effect of interdot coupling affecting the LSPR.[29,44,45] The full wavelength line width at half-maximum of peak spectra ($\Delta\lambda_{fwhm}$) also increases with increasing Au nanodot size (see inset of Figure 3a). It has been demonstrated that the $\Delta\lambda_{fwhm}$ is affected by both radiative and nonradiative damping processes in Au nanoparticles larger than 20−30 nm, and their absolute and relative contributions are both dependent on particle size and material.[15,20−22,28] In our result, the increase of $\Delta\lambda_{fwhm}$ with increasing Au nanodot size indicates that the radiative contribution to the total damping processes is significant for the Au nanodot structure.[21,22,28] In the radiative damping process, the collective electron motion of the LSPR is lost *via* radiation from a time-dependent induced dipole. This radiative damping process depends on the particle volume and the electron density in the metal.[21,28,46,47] Figure 3b shows the difference in absorption between TiO_2-coated 50, 63, and 83 nm Au nanodots on ITO glass and TiO_2-coated ITO glass. For all the TiO_2-coated Au nanodot samples, the λ_{MAX} slightly shifts to the red when the TiO_2 anatase film is coated on the Au nanodots on ITO glass. This red-shift is primarily due to an increase in the dielectric constant of the surrounding medium by coating of TiO_2 (air has a dielectric constant of 1, while the dielectric constant of the TiO_2 layer ranges from 55 to 130 for polycrystalline anatase TiO_2).[43,48] The λ_{MAX} red-shifts and the $\Delta\lambda_{fwhm}$ broadens as the Au nanodot size increases from 50 nm to 83 nm for the TiO_2-coated Au nanodots, which is the same phenomena that was observed for the uncoated Au nanodots. Figure 3c summarizes the results for the Au nanodots and reports the LSPR peak energy (E_{LSPR}) and the LSPR line width (Γ) for Au nanodots. The λ_{MAX} and $\Delta\lambda_{fwhm}$ are converted to E_{LSPR} and Γ using Planck's relation ($E = \hbar c/\lambda$). As shown in Figure 3c, the E_{LSPR} and Γ are a function of the Au nanodot size. These observations could be understood with the red-shift (decrease of E_{LSPR}) and radiative damping process (increase of Γ), which both increased with the Au nanodot size.[15,21,22,28] In addition, it is worthwhile to note that a standard deviation of *ca.* 5% is found for each nanodot sample from the statistical size distributions of Au nanodots (see Figure S3), demonstrating that the observed size effects from UV−vis measurements are not obscured by a varying size distribution. Figure S6 shows spectroradiometer measurement of the light source (Dolan Jenner fiber-optic light source with UV and IR filters) used in this study. The light intensity measured by the spectroradiometer was 122.5 mW/cm^2, which was used for the water splitting reaction.

The TiO_2-coated Au nanodot electrodes were studied for photoelectrochemical water splitting with visible light (light intensity of 122.5 mW/cm^2) in a reactor having three electrodes at room temperature in a 0.1 M KOH solution. Figure 4 shows the current density response of the Au nanodots and the TiO_2-coated Au nanodots with light on/off and an applied anode potential of 0.397 V (*vs* SHE). The theoretical thermodynamic potential for electrochemical water oxidation ($4OH^- \rightarrow 2H_2O + O_2 + 4e^-$) in 0.1 M KOH (pH = 13) is 0.4597 V (*vs* SHE). An applied potential is required for efficient separation of a generated e^-/h^+ pair with light irradiation on the plasmonic catalyst system for the reaction.[23,24,27] We applied a potential of 0.397 V (*vs* SHE) to study the effect of the Au nanodot sizes because electrocatalytic water oxidation does not occur at this potential, thereby allowing us to study the effect of surface plasmons on the photoelectrochemical water splitting reaction. It should be noted that we are reporting the stabilized photocurrent performances with light on/off (see Figure S7). As the Au nanodot size increases from 50 nm to 83 nm, the generated photocurrent with light on decreases (Figure 4a−c). This current increase with light irradiation on the printed Au nanodots may be due to the Ti adhesion layer at the bottom of the printed Au nanodot. A thin Ti layer was introduced to improve the adhesion force of the Au layer to the ITO substrate. It is well known that the Ti metal oxidizes immediately upon exposure to air, and thus the Ti most likely forms TiO_2 under our conditions.[49] Thus, the Au/TiO_2 interface formed around the perimeter of Au nanodots may generate the photocurrent on the Au nanodots. Figure 4d−f show the current response results with light on/off for the water splitting on TiO_2-coated Au nanodots. For all the TiO_2-coated Au nanodot electrodes, the photocurrent response with light on/off increased by about 6 times compared to the Au nanodot alone. This enhancement is probably related to the increased Au/TiO_2 interfacial area. This results in an increased amount of photoinduced charge carriers (e^-/h^+ pair) driving the water splitting reaction that are locally generated at the metal/semiconductor interface due to the local field enhancement near the surface of plasmonic nanoparticles.[23,27] The current produced with visible light increased from 10 to 25 times that of the current produced without visible light, as the Au nanodot size decreased from 83 nm to 50 nm, which is similar to the results for the water splitting on the Au nanodot electrodes. The photocurrent is proportional to the light intensity (with ~1 order dependence) for the TiO_2-coated Au nanodot electrodes, as can be seen from Figure S8. In contrast, the TiO_2-coated electrode without Au nanodot arrays

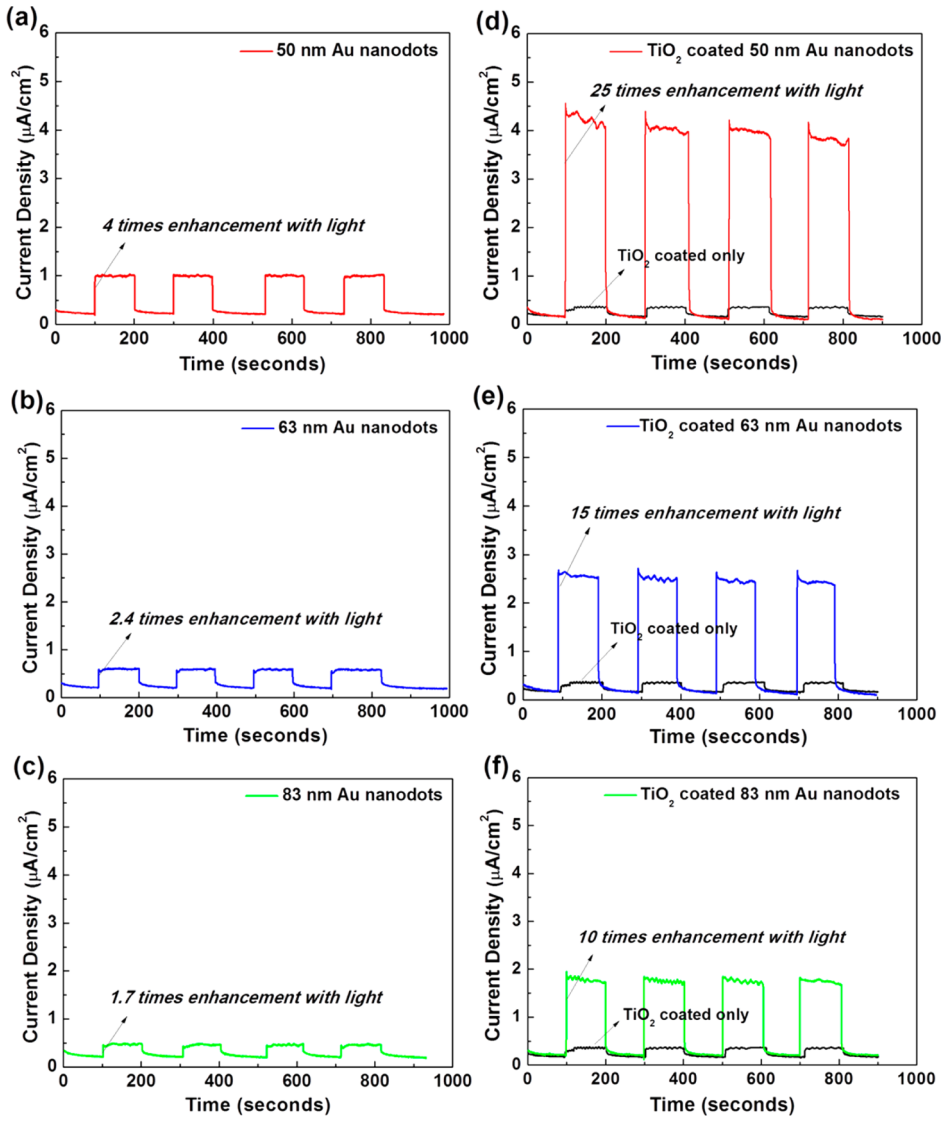

Figure 4. Plasmonic-enhanced water splitting performance at room temperature and a light intensity of 122.5 mW/cm^2. Current density response of (a–c) Au nanodots with different dot sizes (50, 63, 83 nm) and (d–f) the TiO_2-coated Au nanodots according to light on/off at an anode applied potential of 0.397 V (*vs* SHE).

exhibited ~1/2 order dependence of photocurrent with respect to light intensity. It has been demonstrated that the process of direct e^-/h^+ recombination on TiO_2 bulk results in a half-order dependence of the surface concentration of charge carriers on the light intensity.[23,50] This result indicates that the formation of plasmonic metal/semiconductor interfaces by using the well-defined Au nanodot arrays can efficiently enhance the water splitting performance, preventing the e^-/h^+ recombination process.

We have plotted the UV–vis results and photocurrent performances of the Au nanodot in Figure 5. Figure 5a shows the dependence of the radiative damping contribution to the Γ on E_{LSPR} as obtained from the UV–vis measurements and the same data plotted as quality factor. As seen in Figure 5a, the E_{LSPR} decreases and the Γ increases as the Au nanodot size increases from 50 nm to 83 nm. This is probably due to radiative damping (the plasmonic energy loss *via* transformation of particle plasmons into photons).[21,22,28,46,47] Another important parameter follows immediately from the results in Figure 5a, the quality factor of the resonance ($Q = E_{LSPR}/\Gamma$). It has been reported that the quality factor is directly proportional to local field enhancement; large values of quality factor indicate high local field enhancement, and small values mean low local field enhancement.[14,28] The local field enhancement represents the enhancement of the oscillation amplitude of driven amplitude in the case of particle plasmons.[14,21,28] In our results, it is clear that the quality factor increased as the Au nanodot size decreases, which means that the local field enhancement increases with the decreased Au nanodot size from 83 nm to 50 nm. It is noteworthy that the Γ and Q values calculated in this study agree with the theoretical and experimental values reported in the literature.[22,28]

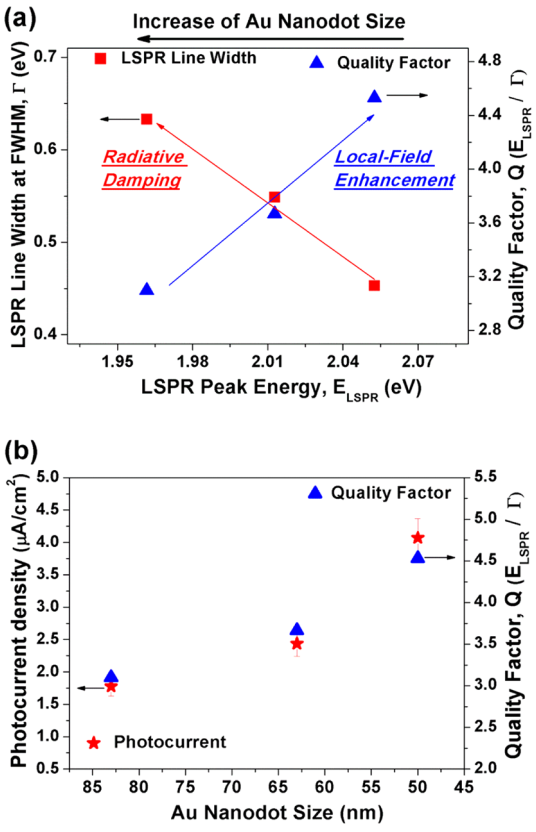

Figure 5. Size effect of Au nanodot arrays for plasmonic-enhanced water splitting. (a) LSPR peak energy (and accordingly nanodot size) dependence of radiative damping contribution to the LSPR line width as obtained from the UV−vis measurements and the same data plotted as quality factor ($Q = E_{LSPR}/\Gamma$). (b) Relation between generated photocurrent at 0.397 V (*vs* SHE) and calculated quality factor (Q) as a function of Au nanodot size.

Figure 5b shows the relation between generated photocurrent for the water splitting and quality factor calculated from UV−vis measurement as a function of Au nanodot size in this study. The photocurrent density increases with decreasing Au nanodot size due to increased local field enhancement as the quality factor increases. It has been reported that the local field enhancement near the surface of plasmonic nanoparticles can increase the e^-/h^+ pair generation rate at the metal/semiconductor interface, increasing the rate of water splitting.[23,27,51] As seen in Figure 5b, both the photocurrent increase (1.8−4.1 μA/cm^2) and the quality factors (3.1−4.5) were systematically changed according to the size of the Au nanodot. It has been reported that spherical Au particles have relatively low quality factors because of interband damping (e^-/h^+ excitations due to transitions between *d* bands of Au and the conduction band) for small particle size and radiation damping for large particle size.[15,21,22,28] In contrast, Sönnichsen *et al.* reported that Au nanorods can have very high quality factors of up to 23 due to the suppressed interband damping.[28] Recently, it has been also demonstrated by Lee *et al.* that the TiO_2-coated Au nanorod structure shows a large photocurrent enhancement for the photoelectrochemical water splitting reaction.[24] In Figure S9, we have plotted the reported quality factor and water splitting performance for Au nanorods from Lee *et al.* with our results for Au nanodots. The photocurrent density for water splitting depends on the quality factor of the plasmonic metal, which in turn depends on the different size and structure of plasmonic metal, as shown in Figure S9. This suggests that the quality factor calculation of the plasmonic nanostructure from absorption or extinction spectra is an important indicator in predicting the performance of plasmonic materials for water splitting reaction and can guide future research in the design of efficient plasmonic catalyst systems for photocatalytic reactions. It has been reported that Ag has higher quality factors than Au in the visible range because interband damping takes place at much higher frequencies than the LSPRs in the case of Ag.[12] The other option is to control the size and structure of the plasmonic metals. The different structures of a plasmonic metal such as nanorods, nanocubes, and nanorings change the LSPR,[15,23,24,28,38] which can increase the quality factor with less damping and a stronger plasmon resonance. However, more theoretical and experimental studies are required to calculate the quality factor of different structures.

Figure 6 shows hydrogen and oxygen production from plasmonic water splitting on 50 nm Au nanodot arrays at room temperature and a light intensity of 122.5 mW/cm^2. The produced hydrogen and oxygen were found by using gas chromatography with a barrier ionization discharge (BID) detector. Figure 6a shows the current density as a function of voltage with light on/off from 0.3 to 1.1 V (*vs* SHE) at a scan rate of 5 mV/s for plasmonic-enhanced water splitting with the TiO_2-coated 50 nm Au nanodot. Initially, we tried to measure the hydrogen production rate at a potential of 0.397 V, where electrocatalytic water oxidation does not occur. At this potential, 40 h reaction was needed to detect the produced hydrogen (see Figure S10) because of the low concentration of hydrogen produced. We increased the applied potential to 0.897 V to measure and compare the hydrogen production rate of the catalyst system for photoelectrochemical water splitting. The amount of hydrogen and oxygen produced as a function of reaction time for the TiO_2-coated 50 nm Au nanodot and only 50 nm Au nanodot with and without light is shown in Figure 6b,c. The experimentally measured ratio of H_2 and O_2 was about 1.6 (±0.2):1, which was close to the stoichiometric ratio of 2:1. The rate of hydrogen production for the water splitting at an applied potential of 0.897 V was about 5 times higher for the TiO_2-coated 50 nm Au nanodot array than the uncoated 50 nm Au nanodot array, as shown in Figure 6d. The 5 times rate enhancement for hydrogen production at 0.897 V was similar to the

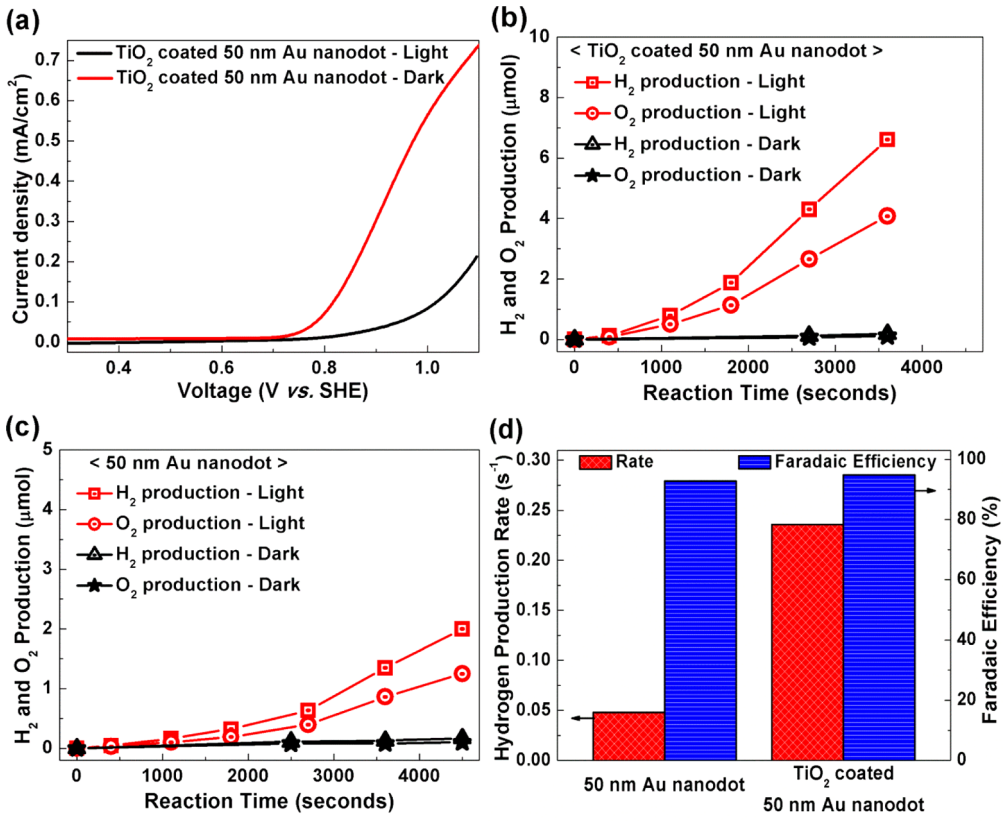

Figure 6. Hydrogen and oxygen production from plasmonic water splitting on 50 nm Au nanodot arrays at room temperature and a light intensity of 122.5 mW/cm^2. (a) Current *vs* voltage profile with light and dark condition from 0.3 to 1.1 V (*vs* SHE) at a scan rate of 5 mV s^{-1} for water splitting. (b) Hydrogen and oxygen production *vs* reaction time on TiO_2-coated 50 nm Au nanodot arrays for water splitting at an applied potential of 0.897 V (*vs* SHE). (c) Hydrogen and oxygen production *vs* reaction time on 50 nm Au nanodot arrays for water splitting at an applied potential of 0.897 V (*vs* SHE). (d) Hydrogen production rate and faradaic efficiency with light irradiation after 1 h time on stream.

6 times photocurrent enhancement at 0.397 V in Figure 4. The Faradaic efficiency was calculated using eq 1. The TiO_2-coated 50 nm Au nanodot and 50 nm Au nanodot array system at 0.897 V had Faradaic efficiencies of 94.9% and 92.8%, respectively, with light irradiation. This indicates that most of the photoinduced charge carriers generated by surface plasmons on Au nanodots with light application participate in the water splitting reaction.

$$\text{Faradaic efficiency} = \frac{nF(\text{mol of hydrogen produced})}{I\Delta t} \quad (1)$$

where I = overall current, Δt = operational time, n = number of electrons participating in the reaction, F = Faraday constant (96 485.34 C/mol), and mol of hydrogen produced = number of moles of hydrogen product.

CONCLUSION

In summary, size-controllable Au nanodot arrays prepared by contact printing technology were used to study the size effect of Au nanodots on water photoelectrolysis. UV−vis absorption spectra showed that the E_{LSPR} decreased and the Γ increased with increased Au nanodot size from 50 nm to 83 nm. The changes of E_{LSPR} and Γ with increasing Au nanodot size in the absorption spectra were due to radiative damping contribution. The current produced with visible light increased from 10 to 25 times that of the current produced without visible light, as the Au nanodot size decreased from 83 nm to 50 nm. The addition of a TiO_2 coating to the Au nanodot array electrodes increased the activity of the nanodots by 6 times for all three nanodot sizes. The activity for water photoelectrolysis is proportional to the quality factor of the catalyst.

EXPERIMENTAL SECTION

Preparation of the CNP Stamps. Fabrication of the controllable CNP stamps begins with formation of porous alumina templates by a general two-step anodization process. First, high-purity (99.999%) Al plates were electrochemically polished in a mixture solution of $HClO_4$ and C_2H_5OH (1:5, v/v) at 0 °C under 15 V for 30 min. The Al sheets were then anodized in a 0.3 M $H_2C_2O_4$

solution at 12 °C under 40 V. After the two-step anodization, pore-widening processes were carried out in etchant solution of H_3PO_4, CrO_3, and DI water (6:1.8:92.2 wt %) at 60 °C. By the pore-widening for 30, 70, and 120 s, AAOs with pore sizes of *ca.* 47, 62, and 82 nm were prepared, respectively, and the pore distance was automatically changed with the pore variation. Next, carbon layers were deposited on the prepared pore channels of the AAOs by a thermal chemical vapor deposition (CVD) method at 600 °C without metal seed layers. A mixed gas flow of C_2H_2 (20 sccm) and NH_3 (80 sccm) was introduced for 6 h as a feedstock for the formation of the carbon layers. Finally, by Ar ion milling followed by chemical wet etching in the etching solution, the vertical CNP arrays were exposed from the AAO surface. The exposed height of the CNP arrays was controlled by a 10 min etching.

Printing of the Au Nanodot Arrays and TiO_2 Film Coating on the Printed Au Nanodot Arrays. To print plasmonic metal nanodot arrays, Au metal layers (*ca.* 12−15 nm) were first deposited on the tips of the CNP arrays by the e-beam evaporation process under a high-vacuum condition of *ca.* 10^{-6} Torr. After loading of the Au layers, a thin Ti adhesion layer (*ca.* 1 nm) was consecutively deposited onto the top of the Au. In this experiment, the deposition rate of the Au and Ti layer was constantly controlled at 0.1 Å/s. The metal-loaded CNP stamps were directly brought into contact with ITO substrates under an applied pressure (0.5−1.0 MPa) for a short time (less than 3 s). After releasing the CNP stamps from the ITO glasses, the Au metal nanodot arrays were finally formed on the substrate.

The TiO_2 layer was coated by dip-coating the Au nanodot printed ITO glass in the prepared TiO_2 sol. Then, the TiO_2-coated Au nanodot electrodes were annealed at 300 °C in an oven for 1 h. The TiO_2 sol was synthesized by hydrolysis of isopropoxide ($Ti(OPr^n)_4$) under acidic conditions followed by the condensation of the hydrolysis products, as reported elsewhere.[52,53]

Reactor Setup and Measurement of Photoelectrochemical Water Splitting Performance. A photoelectrochemical reactor system was designed for studying the plasmonic-enhanced water splitting as shown in Figure 1. The photoelectrochemical reactor is composed of a three-electrode system. A Pt wire and Ag/AgCl (in sat. KCl) are used as counter and reference electrodes, respectively. A metal nanodot-printed transparent ITO glass was used as a working electrode for the plasmonic experiments with a visible light source. The photoelectrochemical water splitting was performed at room temperature in a 0.1 M KOH (pH = 13) solution. Voltage application and current measurements were conducted with a Metrorhm Autolab potentiostat, PGSTAT302N, coupled with a 10 amp current booster, BSTR10A.

For experiments of light on/off and light intensity, a Dolan Jenner fiber-optic light source was used. This source allowed control over the intensity. An EKE 3600 K lamp with UV and IR filters was used as the source of light. The intensity and spectrum of light were measured by a NIST calibrated ILT950 spectroradiometer (see Figure S6). For the accuracy of measurement, the sensor of the spectroradiometer was placed inside the glass reactor to mimic the intensity at the electrode under experimental conditions. Also, using this method, the loss of intensity due to scattering and absorption of the glass reactor wall was taken into consideration.

A septum on the reactor allowed us to sample the gas phase during the reaction. The gas phase was analyzed using a Shimadzu GC-2010 Plus system with the BID detector. Helium was used as the carrier gas in the GC to increase the sensitivity toward H_2 in the BID. A packed RT MS5A column was used to separate the gases. A 500 μL amount of gas sample was injected manually into the GC for quantifying the amount of H_2 and O_2 formed. The GC was calibrated for H_2 and O_2 by injecting different amounts of hydrogen and oxygen and analyzing the peak area.

Conflict of Interest: The authors declare no competing financial interest.

Acknowledgment. This research was funded by the Advanced Research Projects Agency-Energy (ARPA-E), U.S. Department of Energy, under Award Number DE-AR0000329. This work was also supported by the Global Frontier R&D Program on Center for Multiscale Energy System funded by the National Research Foundation (NRF) under the Ministry of Science, ICT & Future Planning, Korea (0420-20130103), an NRF grant funded by the Korea government (MSIP) (No. 2013029776), and the Core Technology Development Program for Next-Generation Solar Cells of Research Institute for Solar and Sustainable Energies (RISE), GIST. We thank Profs. James A. Dumesic, Manos Mavrikakis, and Thomas F. Kuech for helpful discussions.

Supporting Information Available: Characterization of the prepared materials, measurement of photoelectrochemical water splitting performance, and additional figures. This material is available free of charge *via* the Internet at http://pubs.acs.org.

REFERENCES AND NOTES

1. Fujishima, A.; Honda, K. Electrochemical Photolysis of Water at a Semiconductor Electrode. *Nature* **1972**, *238*, 37.
2. Walter, M. G.; Warren, E. L.; McKone, J. R.; Boettcher, S. W.; Mi, Q. X.; Santori, E. A.; Lewis, N. S. Solar Water Splitting Cells. *Chem. Rev.* **2010**, *110*, 6446–6473.
3. Chen, X. B.; Shen, S. H.; Guo, L. J.; Mao, S. S. Semiconductor-Based Photocatalytic Hydrogen Generation. *Chem. Rev.* **2010**, *110*, 6503–6570.
4. Warren, S. C.; Voitchovsky, K.; Dotan, H.; Leroy, C. M.; Cornuz, M.; Stellacci, F.; Hebert, C.; Rothschild, A.; Gratzel, M. Identifying Champion Nanostructures for Solar Water-Splitting. *Nat. Mater.* **2013**, *12*, 842–849.
5. Kargar, A.; Sun, K.; Jing, Y.; Choi, C.; Jeong, H.; Jung, G. Y.; Jin, S.; Wang, D. L. 3D Branched Nanowire Photoelectrochemical Electrodes for Efficient Solar Water Splitting. *ACS Nano* **2013**, *7*, 9407–9415.
6. Kargar, A.; Jing, Y.; Kim, S. J.; Riley, C. T.; Pan, X. Q.; Wang, D. L. ZnO/CuO Heterojunction Branched Nanowires for Photoelectrochemical Hydrogen Generation. *ACS Nano* **2013**, *7*, 11112–11120.
7. Linic, S.; Christopher, P.; Ingram, D. B. Plasmonic-Metal Nanostructures for Efficient Conversion of Solar to Chemical Energy. *Nat. Mater.* **2011**, *10*, 911–921.
8. Warren, S. C.; Thimsen, E. Plasmonic Solar Water Splitting. *Energy Environ. Sci.* **2012**, *5*, 5133–5146.
9. Hou, W. B.; Cronin, S. B. A Review of Surface Plasmon Resonance-Enhanced Photocatalysis. *Adv. Funct. Mater.* **2013**, *23*, 1612–1619.
10. Zhang, X. M.; Chen, Y. L.; Liu, R. S.; Tsai, D. P. Plasmonic Photocatalysis. *Rep. Prog. Phys.* **2013**, *76*, 046401.
11. Kale, M. J.; Avanesian, T.; Christopher, P. Direct Photocatalysis by Plasmonic Nanostructures. *ACS Catal.* **2013**, *4*, 116–128.
12. Halas, N. J. Plasmonics: An Emerging Field Fostered by Nano Letters. *Nano Lett.* **2010**, *10*, 3816–3822.
13. Halas, N. J.; Lal, S.; Chang, W. S.; Link, S.; Nordlander, P. Plasmons in Strongly Coupled Metallic Nanostructures. *Chem. Rev.* **2011**, *111*, 3913–3961.
14. Rycenga, M.; Cobley, C. M.; Zeng, J.; Li, W.; Moran, C. H.; Zhang, Q.; Qin, D.; Xia, Y. Controlling the Synthesis and Assembly of Silver Nanostructures for Plasmonic Applications. *Chem. Rev.* **2011**, *111*, 3669–3712.
15. Link, S.; El-Sayed, M. A. Spectral Properties and Relaxation Dynamics of Surface Plasmon Electronic Oscillations in Gold and Silver Nanodots and Nanorods. *J. Phys. Chem. B* **1999**, *103*, 8410–8426.
16. Link, S.; El-Sayed, M. A. Size and Temperature Dependence of the Plasmon Absorption of Colloidal Gold Nanoparticles. *J. Phys. Chem. B* **1999**, *103*, 4212–4217.
17. Kelly, K. L.; Coronado, E.; Zhao, L. L.; Schatz, G. C. The Optical Properties of Metal Nanoparticles: The Influence of Size, Shape, and Dielectric Environment. *J. Phys. Chem. B* **2003**, *107*, 668–677.
18. Jain, P. K.; Lee, K. S.; El-Sayed, I. H.; El-Sayed, M. A. Calculated Absorption and Scattering Properties of Gold Nanoparticles of Different Size, Shape, and Composition: Applications in Biological Imaging and Biomedicine. *J. Phys. Chem. B* **2006**, *110*, 7238–7248.

19. Langhammer, C.; Yuan, Z.; Zoric, I.; Kasemo, B. Plasmonic Properties of Supported Pt and Pd Nanostructures. *Nano Lett.* **2006**, *6*, 833–838.
20. Langhammer, C.; Kasemo, B.; Zoric, I. Absorption and Scattering of Light by Pt, Pd, Ag, and Au Nanodisks: Absolute Cross Sections and Branching Ratios. *J. Chem. Phys.* **2007**, *126*, 194702.
21. Zoric, I.; Zach, M.; Kasemo, B.; Langhammer, C. Gold, Platinum, and Aluminum Nanodisk Plasmons: Material Independence, Subradiance, and Damping Mechanisms. *ACS Nano* **2011**, *5*, 2535–2546.
22. Sonnichsen, C.; Franzl, T.; Wilk, T.; von Plessen, G.; Feldmann, J. Plasmon Resonances in Large Noble-Metal Clusters. *New J. Phys.* **2002**, *4*, 93.
23. Ingram, D. B.; Linic, S. Water Splitting on Composite Plasmonic-Metal/Semiconductor Photoelectrodes: Evidence for Selective Plasmon-Induced Formation of Charge Carriers near the Semiconductor Surface. *J. Am. Chem. Soc.* **2011**, *133*, 5202–5205.
24. Lee, J.; Mubeen, S.; Ji, X. L.; Stucky, G. D.; Moskovits, M. Plasmonic Photoanodes for Solar Water Splitting with Visible Light. *Nano Lett.* **2012**, *12*, 5014–5019.
25. DeSario, P. A.; Pietron, J. J.; DeVantier, D. E.; Brintlinger, T. H.; Stroud, R. M.; Rolison, D. R. Plasmonic Enhancement of Visible-Light Water Splitting with Au-TiO_2 Composite Aerogels. *Nanoscale* **2013**, *5*, 8073–8083.
26. Zhang, Z. H.; Zhang, L. B.; Hedhili, M. N.; Zhang, H. N.; Wang, P. Plasmonic Gold Nanocrystals Coupled with Photonic Crystal Seamlessly on TiO_2 Nanotube Photoelectrodes for Efficient Visible Light Photoelectrochemical Water Splitting. *Nano Lett.* **2013**, *13*, 14–20.
27. Liu, Z. W.; Hou, W. B.; Pavaskar, P.; Aykol, M.; Cronin, S. B. Plasmon Resonant Enhancement of Photocatalytic Water Splitting under Visible Illumination. *Nano Lett.* **2011**, *11*, 1111–1116.
28. Sonnichsen, C.; Franzl, T.; Wilk, T.; von Plessen, G.; Feldmann, J.; Wilson, O.; Mulvaney, P. Drastic Reduction of Plasmon Damping in Gold Nanorods. *Phys. Rev. Lett.* **2002**, *88*, 077402.
29. Vazquez-Mena, O.; Sannomiya, T.; Villanueva, L. G.; Voros, J.; Brugger, J. Metallic Nanodot Arrays by Stencil Lithography for Plasmonic Biosensing Applications. *ACS Nano* **2011**, *5*, 844–853.
30. Watanabe, K.; Menzel, D.; Nilius, N.; Freund, H. J. Photochemistry on Metal Nanoparticles. *Chem. Rev.* **2006**, *106*, 4301–4320.
31. Murdoch, M.; Waterhouse, G. I. N.; Nadeem, M. A.; Metson, J. B.; Keane, M. A.; Howe, R. F.; Llorca, J.; Idriss, H. The Effect of Gold Loading and Particle Size on Photocatalytic Hydrogen Production from Ethanol over Au/TiO_2 Nanoparticles. *Nat. Chem.* **2011**, *3*, 489–492.
32. Rogers, J. A.; Nuzzo, R. G. Recent Progress in Soft Lithography. *Mater. Today* **2005**, *8*, 50–56.
33. Zaumseil, J.; Meitl, M. A.; Hsu, J. W. P.; Acharya, B. R.; Baldwin, K. W.; Loo, Y. L.; Rogers, J. A. Three-Dimensional and Multilayer Nanostructures Formed by Nanotransfer Printing. *Nano Lett.* **2003**, *3*, 1223–1227.
34. Cao, T. B.; Xu, Q. B.; Winkleman, A.; Whitesides, G. M. Fabrication of Thin, Metallic Films along the Sidewalls of a Topographically Patterned Stamp and Their Application in Charge Printing. *Small* **2005**, *1*, 1191–1195.
35. Xia, Y. N.; Whitesides, G. M. Soft Lithography. *Angew. Chem., Int. Ed.* **1998**, *37*, 551–575.
36. Lee, S. H.; Jo, G.; Park, W.; Lee, S.; Kim, Y.-S.; Cho, B. K.; Lee, T.; Kim, W. B. Diameter-Engineered SnO_2 Nanowires over Contact-Printed Gold Nanodots Using Size-Controlled Carbon Nanopost Array Stamps. *ACS Nano* **2010**, *4*, 1829–1836.
37. Lee, S. H.; Cho, B.; Yoon, S.; Jeong, H.; Jon, S.; Jung, G. Y.; Cho, B. K.; Lee, T.; Kim, W. B. Printing of Sub-100-nm Metal Nanodot Arrays by Carbon Nanopost Stamps. *ACS Nano* **2011**, *5*, 5543–5551.
38. Lee, S. H.; Yoon, S.; Jeong, H.; Han, M.; Choi, S. M.; Kim, J. G.; Park, J.-W.; Jung, G. Y.; Cho, B. K.; Kim, W. B. Printable Nanoscale Metal Ring Arrays *via* Vertically Aligned Carbon Nanotube Platforms. *Nanoscale* **2013**, *5*, 10653–10659.
39. Loo, Y. L.; Willett, R. L.; Baldwin, K. W.; Rogers, J. A. Additive, Nanoscale Patterning of Metal Films with a Stamp and a Surface Chemistry Mediated Transfer Process: Applications in Plastic Electronics. *Appl. Phys. Lett.* **2002**, *81*, 562–564.
40. Yu, J. G.; Zhao, X. J.; Zhao, Q. N. Photocatalytic Activity of Nanometer TiO_2 Thin Films Prepared by the Sol-Gel Method. *Mater. Chem. Phys.* **2001**, *69*, 25–29.
41. Kim, D. J.; Hahn, S. H.; Oh, S. H.; Kim, E. J. Influence of Calcination Temperature on Structural and Optical Properties of TiO_2 Thin Films Prepared by Sol-Gel Dip Coating. *Mater. Lett.* **2002**, *57*, 355–360.
42. Lee, S.; Cho, I. S.; Lee, J. H.; Kim, D. H.; Kim, D. W.; Kim, J. Y.; Shin, H.; Lee, J. K.; Jung, H. S.; Park, N. G.; Kim, K.; Ko, M. J.; Hong, K. S. Two-Step Sol-Gel Method-Based TiO_2 Nanoparticles with Uniform Morphology and Size for Efficient Photo-Energy Conversion Devices. *Chem. Mater.* **2010**, *22*, 1958–1965.
43. Anker, J. N.; Hall, W. P.; Lyandres, O.; Shah, N. C.; Zhao, J.; Van Duyne, R. P. Biosensing with Plasmonic Nanosensors. *Nat. Mater.* **2008**, *7*, 442–453.
44. Danckwerts, M.; Novotny, L. Optical Frequency Mixing at Coupled Gold Nanoparticles. *Phys. Rev. Lett.* **2007**, *98*, 026104.
45. Sannomiya, T.; Sahoo, P. K.; Mahcicek, D. I.; Solak, H. H.; Hafner, C.; Grieshaber, D.; Voeroes, J. Biosensing by Densely Packed and Optically Coupled Plasmonic Particle Arrays. *Small* **2009**, *5*, 1889–1896.
46. Perner, M.; Bost, P.; Lemmer, U.; vonPlessen, G.; Feldmann, J.; Becker, U.; Mennig, M.; Schmitt, M.; Schmidt, H. Optically Induced Damping of the Surface Plasmon Resonance in Gold Colloids. *Phys. Rev. Lett.* **1997**, *78*, 2192–2195.
47. Wokaun, A.; Gordon, J. P.; Liao, P. F. Radiation Damping in Surface-Enhanced Raman-Scattering. *Phys. Rev. Lett.* **1982**, *48*, 957–960.
48. Mubeen, S.; Hernandez-Sosa, G.; Moses, D.; Lee, J.; Moskovits, M. Plasmonic Photosensitization of a Wide Band Gap Semiconductor: Converting Plasmons to Charge Carriers. *Nano Lett.* **2011**, *11*, 5548–5552.
49. Munoz-Portero, M. J.; Garcia-Anton, J.; Guinon, J. L.; Leiva-Garcia, R. Pourbaix Diagrams for Titanium in Concentrated Aqueous Lithium Bromide Solutions at 25 Degrees C. *Corros. Sci.* **2011**, *53*, 1440–1450.
50. Yates, J. T. Photochemistry on TiO_2: Mechanisms behind the Surface Chemistry. *Surf. Sci.* **2009**, *603*, 1605–1612.
51. Awazu, K.; Fujimaki, M.; Rockstuhl, C.; Tominaga, J.; Murakami, H.; Ohki, Y.; Yoshida, N.; Watanabe, T. A Plasmonic Photocatalyst Consisting of Sliver Nanoparticles Embedded in Titanium Dioxide. *J. Am. Chem. Soc.* **2008**, *130*, 1676–1680.
52. Vichi, F. M.; Tejedor-Tejedor, M. I.; Anderson, M. A. Effect of Pore-Wall Chemistry on Proton Conductivity in Mesoporous Titanium Dioxide. *Chem. Mater.* **2000**, *12*, 1762–1770.
53. Xu, Q. Y.; Anderson, M. A. Synthesis of Porosity Controlled Ceramic Membranes. *J. Mater. Res.* **1991**, *6*, 1073–1081.